applied sciences

MDPI

Article

Cable-Driven Mechanism Models for Sensitive and Actuated Minimally Invasive Robotic Instruments

Giovanni Gerardo Muscolo * **and Paolo Fiorini**

Department of Engineering for Innovation Medicine, Section of Engineering and Physics, University of Verona, Ca' Vignal 2-Strada Le Grazie 15, 37134 Verona, Italy; paolo.fiorini@univr.it
* Correspondence: giovannigerardo.muscolo@univr.it

Abstract: Cable-driven mechanism models are, usually, included in actuated systems; however, recently, their use for sensitive systems has been explored. In this paper, two cable-driven multi-body mechanism models are compared, underlining advantages and constraints in using sensitive cable-driven mechanisms for minimally invasive robotic instruments. The proposed approach could be useful in bypassing sterilization problems for surgical robotic instruments because our system allows for the separation of the robotic sterilizable part from the sensitive-actuated part of the surgical instrument. The real implementation of the proposed mechanism models, presented partially in other works, are validated in this paper, performing a simulation using a multi-body environment. Results confirm the feasibility of the proposed sensitive-actuated approach, defining new bases for the next challenges of the future.

Keywords: cable-driven systems; surgical robotics; compliant mechanisms; sensitive mechanisms; minimally invasive surgical robotic tools; minimally invasive robotic instruments

check for updates

Citation: Muscolo, G.G.; Fiorini, P. Cable-Driven Mechanism Models for Sensitive and Actuated Minimally Invasive Robotic Instruments. *Appl. Sci.* **2024**, *14*, 2951. https://doi.org/10.3390/app14072951

Academic Editor: Marco Troncossi

Received: 20 February 2024
Revised: 19 March 2024
Accepted: 29 March 2024
Published: 31 March 2024

1. Introduction

Classical surgery is performed by the surgeon's team, opening the body of the patient, in order to enter in the human body and to remove cancers or to perform other operations [1,2]. Classical surgery includes many limits for the health of patients, during and after surgery [2]. Hemorrhages and bleeding occur more often in classical surgery than in robotic surgery. One reason for this is because the patient's body is opened. On the contrary, in robot-assisted surgery, only a few small incisions on the patient's body are performed to insert the tools in the body. This approach of robotic surgery is called minimally invasive robotic surgery [3–5]. An additional advantage of robot-assisted surgery is to reduce hand tremor, which can be transferred from the surgeon's hands to the patient's body in classical surgery.

Robotic surgery is carried out using two robotic structures that ensure the physical separation of patients and surgeons (see Figure 1): a local (near the surgeon) and a remote station (near the patient) [4]. The remote part consists of robotic arms with minimally invasive robotic tools (or instruments) (MIRIs) (see Figure 2), controlled in teleoperation by the local part. The MIRIs (in the remote part), enter into the patient's body, and the surgeon (in the local part) controls their motions with her/his hands. Normally, the local station is equipped only with visual feedback for the surgeon. The tip of the MIRI can be constituted by forceps used for cutting, or tools for suturing or grasping, actuated by cable-driven systems [3,4]. Figure 2 shows the da Vinci Research Kit (dVRK), available at the University of Verona (Italy). In the local station, the surgeon can interact using feet and hands with the console of the surgical robot. The surgeon has a view of the internal body of the patient because the endoscope (in the remote robot) is inside the patient's body, and it consists of a stereo camera. The remote instruments normally include two MIRIs. In dVRK, the cables of the MIRIs are connected to forceps on the tip and to four pulleys on the base, as shown in Figure 2. The four pulleys of MIRIs are connected to four motors on the remote robotic arm.

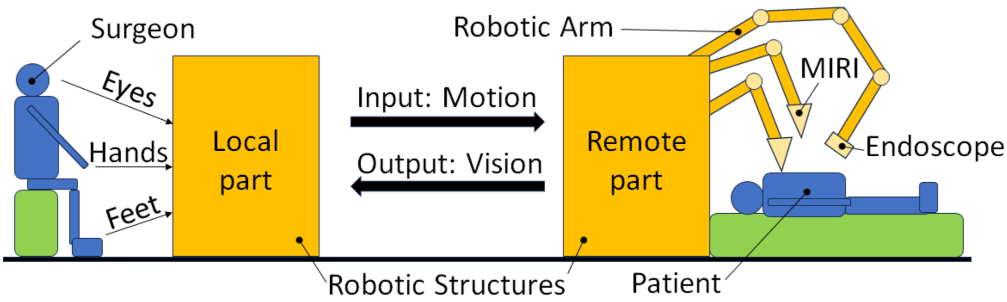

Figure 1. Telerobotic Surgical System.

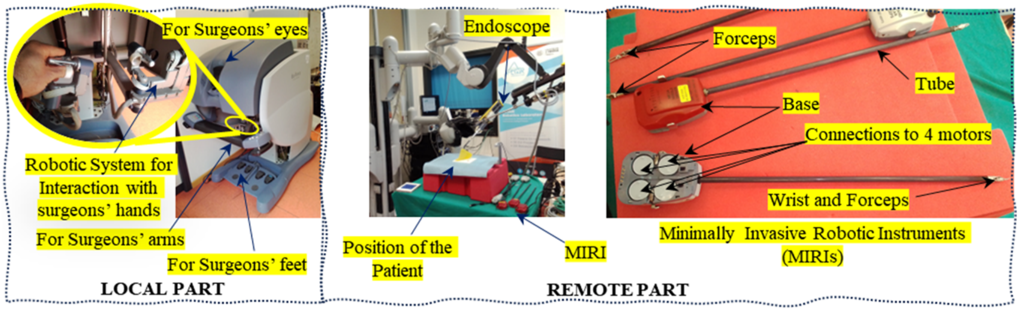

Figure 2. Da Vinci Research Kit (dVRK) (courtesy of the University of Verona): Local Part and Remote Part.

The da Vinci robotic arm is an example of a cable-driven actuated system. This type of solution is useful when the robot end-effector must be very light. Motors are positioned away from the instruments, and the cables produce the end-effectors' motions. Many cable-driven actuated solutions are available in the literature for bio-robotic arms [6], robotic rehabilitation [7], building constructions [8], and many other applications [9–11].

Recently, a new cable-driven sensitive approach has been conceived, in which tension on cables are used to measure forces on the mobile part connected to the fixed part by using cables. Our past works, ref. [5] and ref. [12], focused on this new research direction [13–19]. Some recent work measures the tension on cables, in which the fixed part has bigger dimensions than the mobile part [15,19]. Considering an application to MIRIs, our solution has a different approach: the fixed part has a smaller diameter with respect to the diameter of the MIRI and to the mobile part. In this paper, a comparison between our proposed solutions with different macroscopic and miniaturized scales is presented.

One important problem in robotic surgery architectures is that tactile feedback is very difficult to implement on MIRIs. In order to increase surgeons' capabilities to carry out surgical operations, tactile information must be transferred to surgeons' hands [3–5]. Some critical points preventing the use of tactile/haptic feedback in robot-assisted surgery are:

- The small dimension of MIRIs (the diameter of the tube, shown in Figure 2, is around 8 mm);
- The MIRI sterilization that limits the life of electronic components in the sensing system (e.g., Micro-Electro-Mechanical Systems sensors [12], which could be included in MIRIs to measure a tactile interaction with the tissues [4]);
- Errors during the motion of forceps [3];
- The communication delay between the motion of surgeons' hands and the motion of MIRIs may limit perception and induce instability [3–5];
- The small forces generated by sensors, especially when using MEMS sensors [12].

A detailed analysis on the surgical robotic instruments state of the art (published in [4]) underlined that surgeons with experience in robotic surgery are able to perform different tasks, and force feedback (FF) and haptic feedback (HF) from robotic surgical tools help novices to reduce forces on the human tissue, avoiding dangerous situations. If economically and technically feasible, FF and HF from surgical instruments could help experts and novices to increase the quality of surgical operations [20].

The dexterity of MIRIs is increased when adopting bending mechanisms, such as the one proposed in [21]. The cable-driven mechanism is used to actuate the MIRI and the bending mechanism, in the base of its design, and allows for the performance of predefined movements modifying the workspace. The bending mechanism is positioned between the end of the tube and the forceps, replacing the wrist of the dVRK MIRI. The same location between the tube and the forceps is used to include the continuum wrist proposed in [22].

One important aspect to consider is the misalignment between the command given by the local part and the motion performed by the MIRI. In [23], the misalignment is evaluated, underlining that users were able to compensate for misalignment angles up to approximately 20 degrees in both tool orientation and camera viewpoint misalignment.

Cable-driven systems are used in the design of minimally invasive robotic surgery. The robotic arm of dVRK, shown in Figure 2, is an example of a robot designed with cable-driven instruments, such as MIRIs shown in the same figure. Many examples like this are available in the literature, such as in [24]. A very interesting surgical instrument is shown in [25], in which CYCLOPS is presented: a robotic tool for endoscopic surgery based on the concept of tendon-driven parallel robots. The cable-driven concept proposed in the paper is in the same line of the one we published in [5], using cables to move a mobile part with respect to the fixed part and with a direct force mapping principle involved, but applied with different methods and design. Other solutions are tested to include force-torque sensors in MIRIs, such as the one included in [26], in which fiber Bragg gratings (FBG) are used. FBG have many advantages, such as immunity to electromagnetic interference, light weight, etc.; however, severe cross sensitivities and high non-linearities are common drawbacks, as underlined in [26].

New sensorized MIRIs must be studied and designed to reduce excessive tool–tissue interaction forces, which often result in tissue damage, as underlined in a recent review paper [27]. FBG [26,28], capacitive sensors [29,30], and strain-gauges [31] are only some of the sensing elements available for MEMS and MIRIs, as shown in [4,32]. The sensitive element can be positioned in the sterilized workspace, but in this case, the electronic components of the sensor can be damaged by sterilization. Another approach is to position the sensor outside the sterilized zone, such as the work proposed in [33]. However, problems of communication, sensitivity, and errors are more evident in this case because the zone of the interaction forces is not near the position where the sensor is located.

In this paper, we propose the design and control of new sensitive-actuated models for MIRIs. Our objective is to give to the research community of surgical robotics new types of MIRIs that are able to transfer and measure high forces, but also to bypass the problems caused by sterilization. In our sensitive approach, the sterilized forceps, conceived without electronic components, Micro-Electro-Mechanical-Systems (MEMS), or sensors, inside it, will be in contact with the human body. The cable-driven system is used to transfer the measure of the bending motion of the MIRI from the tip of the instrument to its base. The measure of the bending motion in the base gives the measure of forces and displacements in the tip of the MIRI. By using our sensitive approach, the MIRI can be sterilized because it is not built with sensors and electronic components (such as PCBs, MEMS, etc.), but the cable connection gives the information of the mechanical behavior of the tip directly to the sensors' base.

Recently, we published a paper in which we proposed and validated a mechanism model and general formulations, using two test benches for experimentation [5]. Another simplified mechanism model with a new formulation was validated in a virtual multi-body model and tested in a planar test bench for experimentation [12].

In this paper, we perform a critical analysis on our sensitive approach for MIRIs, comparing two models (MM1 and MM2) presented in part in other works ([5]). The results presented in [5] with the implementation of the proposed formula (MM2) in two real test benches is also confirmed and validated in this paper, including a new multi-physics simulation. A comparison of the two mechanism models (MM1 and MM2) gives a general overview on the feasibility of the approach we propose in bypassing the problem of sterilization in surgical robotics.

The paper is structured as follows: Section 2 shows formulations used for the definition of the mechanism models; Section 3 shows an overview of the physical implementation of one mechanism model; Section 4 shows the design and control of multi-body models conceived and simulated in this paper; Section 5 shows the results and discussion. The paper ends with the conclusions.

2. Modeling of Sensitive Cable-Driven Mechanisms

2.1. Cable-Driven Sensitive Models

The basic idea of our invention is to design the sensitive mechanism composed of two parts: the mobile part (A) and fixed part (B), shown in Figure 3. Part B is fixed to part D of the MIRI, and part A is fixed to part C (connected to the forceps). In order to simplify the discussion in this document, the general behavior of models is shown in a plane, but applications and implementations have been performed in a plane and space, as can be shown in [5].

The motion of part A with respect to part B is performed by using cables. Figure 4 shows the general scheme used for two different cable-driven mechanism models (MM1 left and MM2 right), presented for the first time in [5]. In Figure 4, tensions on cables are shown from $\mathbf{T}_{10}$ to $\mathbf{T}_{80}$. Anchor points of cables with the mobile part A are shown with red points. In each model (MM1 or MM2), eight cables are used; however, the substantial difference between the two mechanism models can be shown by analyzing Figure 4. The formulation (conceived and presented in [5]) allows for the reconstruction of the motion of part A, measuring and synchronizing the elongation and shortening of a spring at the end of each cable. Thanks to the measure of the stiffness coefficient of each spring, it is also possible to measure the external load applied on part A.

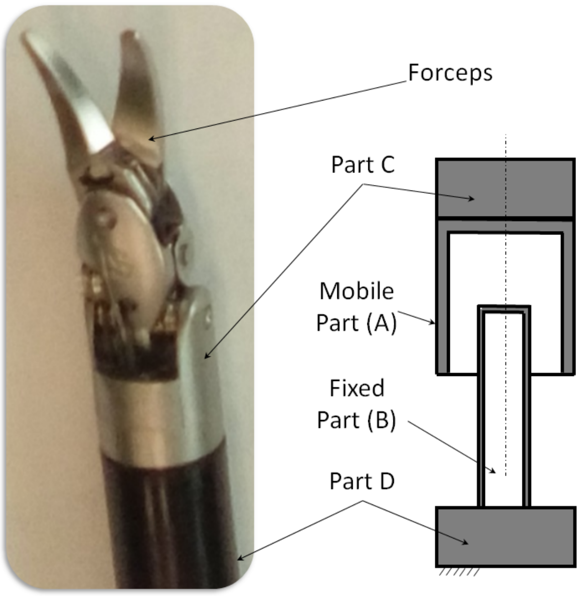

Figure 3. Minimally invasive robotic instrument (MIRI) (**left**) and sketch of the planar section (**right**).

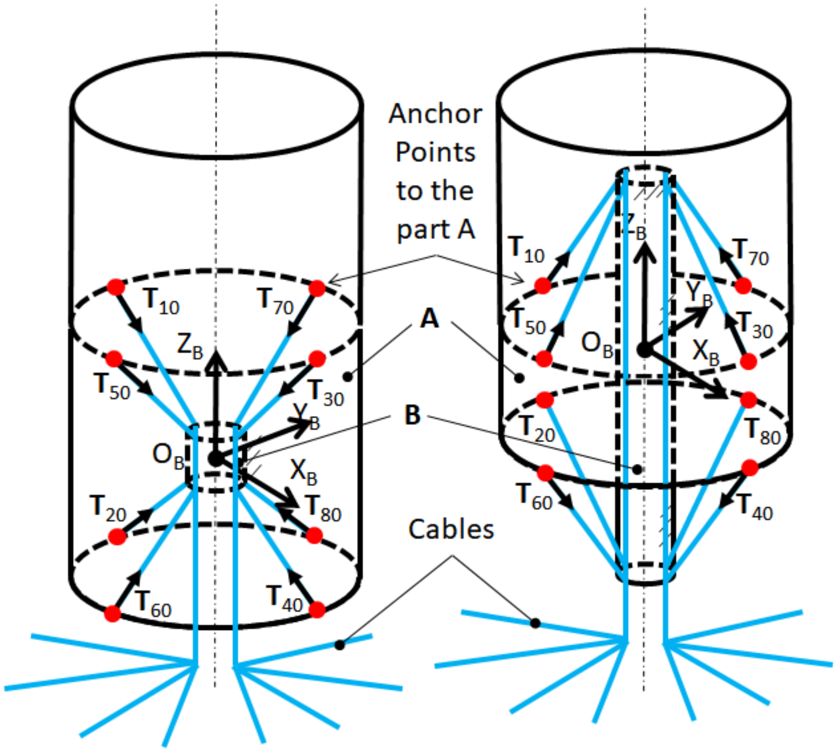

Figure 4. Sketches of two different sensitive cable-driven mechanism models (left: MM1; right: MM2), presented for the first time in [5]. Tensions on cables are shown from $\mathbf{T}_{10}$ to $\mathbf{T}_{80}$. Anchor points of cables with mobile part A are shown in red.

Figure 5 shows the planar section of the two sensitive cable-driven mechanism models (MM1 on left, MM2 on right), presented in [5]. The two models were conceived to measure the forces and torques on part C connected to the forceps (by using cables) during the interaction with the environment.

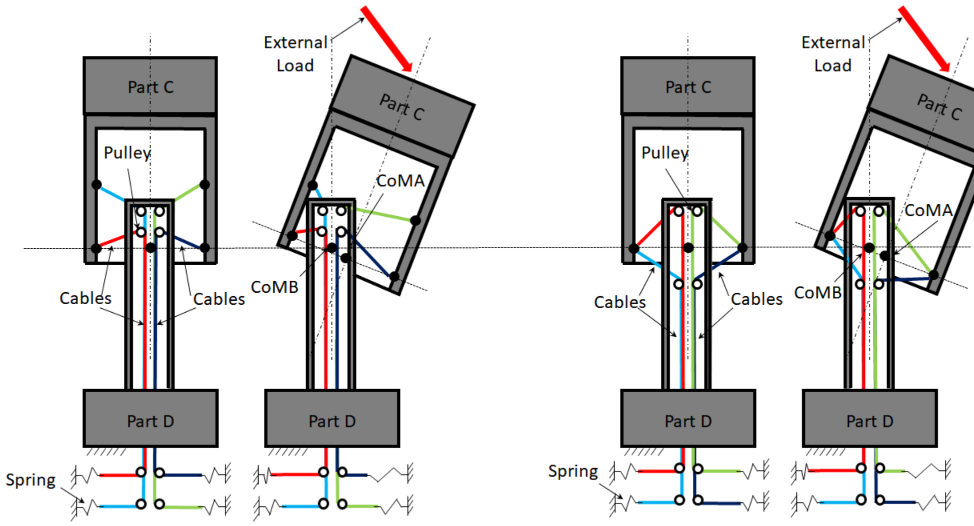

Figure 5. Planar section of sensitive cable-driven mechanism models (MM1 on left and MM2 on right), introduced in [5]. CoMA and CoMB are the centers of mass, respectively, of mobile part A and fixed part B.

Another simplified sensitive cable-driven mechanism model (MM3), with motion in a plane, and validated algorithms to measure forces and displacements were presented in [12]. Figure 6 shows a section of the planar model MM3. A revolute joint in *O* allows for the performance of the motion of the planar system with 1 degree of freedom and for the measurement of external loads and displacements by using only two cables. More details on this mechanism model can be shown in [12].

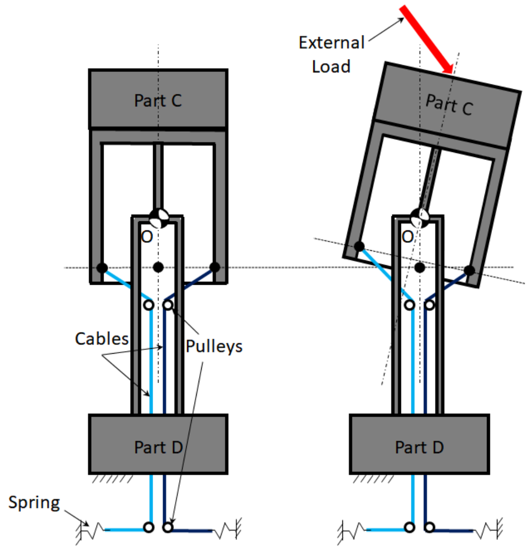

Figure 6. Section of the Planar Sensitive Cable-Driven Mechanism Model with 1 degree of freedom and two cables, presented in [12] (MM3).

2.2. General Algorithms and Formulations

Figure 7 shows the general scheme used to determine three cable-driven mechanism models presented in [5] (MM1 and MM2) and in [12] (MM3).

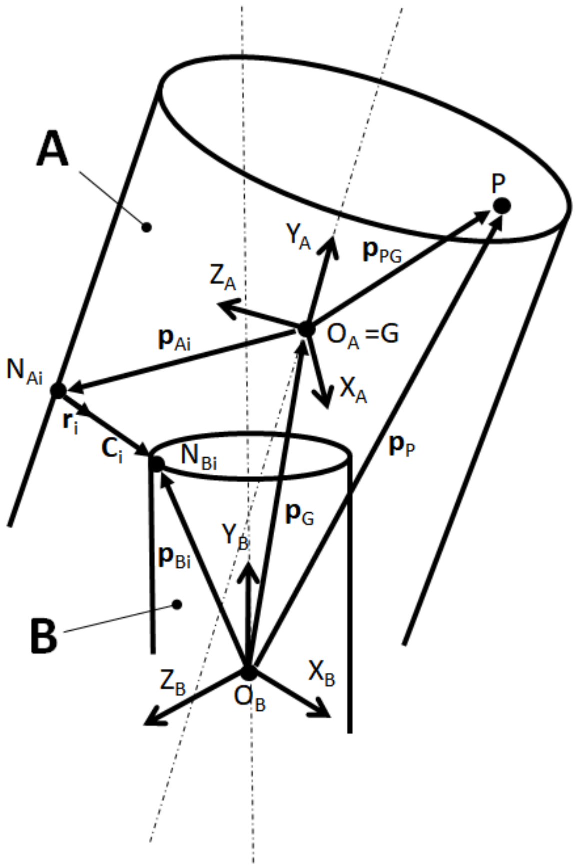

Figure 7. General scheme used to determine cable-driven mechanism models presented in [5] (MM1 and MM2) and [12] (MM3).

$O_A - X_AY_AZ_A$ is the reference system of mobile part A, and $O_B - X_BY_BZ_B$ is the reference system of fixed part B, each one applied in its center of mass. N_{Bi} and N_{Ai} are anchor points of the cables, respectively, connected to part B and part A. $\mathbf{p}_{Bi}$ and $\mathbf{p}_{Ai}$ are position vectors. The vector of the cables is $\mathbf{C}_i$, and $\mathbf{r}_i$ is the unit vector of the cables. $\mathbf{p}_G$ is the position vector of mobile platform A with respect to fixed platform B. $\mathbf{p}_P$ and $\mathbf{p}_{PG}$ are position vectors of the general point P with respect to the reference systems of the fixed (B) and mobile (A) parts.

The correlation among the length of cables ($\mathbf{C}_i$), the position vectors of anchor points ($\mathbf{p}_{Bi}$ and $\mathbf{p}_{Ai}$), and the position vector of mobile part A with respect to fixed part B ($\mathbf{p}_G$) is shown by the following equations for eight cables, including the rotational matrix S to transform the vectors calculated in mobile platform A with respect to fixed platform B:

$$\mathbf{C}_i = +\mathbf{p}_{Bi} - \mathbf{p}_G - \mathbf{S}\mathbf{p}_{Ai}; i = 1, ..., 8; \tag{1}$$

$\sum_{i=1}^{8} \mathbf{T}_i = \sum_{i=1}^{8} T_i\mathbf{r}_i$ are tensions on the cables applied to mobile platform A in N_{Ai}; $\sum_{i=1}^{8} (\mathbf{S}\mathbf{p}_{Ai} \wedge \mathbf{T}_i)$ are torques produced by tensions on the cables; $m\mathbf{g}_G$ is gravity; $\mathbf{F}_P$ and $\mathbf{M}_P$ are, respectively, the external forces and torques applied to point P shown in Figure 7:

$$\begin{bmatrix} \mathbf{r}_1 & \dots & \mathbf{r}_8 \\ \mathbf{S}\mathbf{p}_{A1} \wedge \mathbf{r}_1 & \dots & \mathbf{S}\mathbf{p}_{A8} \wedge \mathbf{r}_8 \end{bmatrix} \begin{bmatrix} T_1 \\ \vdots \\ T_8 \end{bmatrix} = -\begin{bmatrix} m\mathbf{g}_G \\ (\mathbf{p}_G \wedge m\mathbf{g}_G) \end{bmatrix} - \begin{bmatrix} \mathbf{F}_P \\ (\mathbf{p}_P \wedge \mathbf{F}_P) + \mathbf{M}_P \end{bmatrix} \tag{2}$$

$$\mathbf{Q}\mathbf{T} = -\mathbf{U}_G - \mathbf{U}_P \tag{3}$$

where $\mathbf{Q}$ is the force transformation matrix [34]; $\mathbf{T}$ is the vector of the cables' tension; $\mathbf{U}_G$ is the gravity vector [15]. The vector of external forces and torques, applied to point P ($\mathbf{U}_P$), is calculated by the analysis of variation of the tension of cables $\Delta\mathbf{T} = \mathbf{T}_1 - \mathbf{T}_0$; $\mathbf{T}_0$ is the vector of the tension on the cables used as an offset in the starting balancing configuration, and $\mathbf{T}_1$ is the vector of the tension on the cables in the new balancing configuration:

$$\mathbf{U}_P = \left[F_{PX}, F_{PY}, F_{PZ}, M_{PX}, M_{PY}, M_{PZ}\right]^T = \mathbf{U}_{P0} - \mathbf{Q}\Delta\mathbf{T} \tag{4}$$

$\mathbf{U}_{P0}$ is the vector of external forces and torques in the starting balancing configuration. In our models, we used $\mathbf{U}_{P0} = 0$, and Equation (4) can be rewritten with the following Equation (5). All details of the used formulations and models can be found in [5,12].

$$\mathbf{U}_P = \left[F_{PX}, F_{PY}, F_{PZ}, M_{PX}, M_{PY}, M_{PZ}\right]^T = -\mathbf{Q}\Delta\mathbf{T} \tag{5}$$

2.3. Modeling of the Mechanism Model MM1

The general mechanical behavior of the three mechanism models (MM1, MM2, and MM3) is described with the formulations presented above. The mechanism models MM1 and MM2 (shown in Figures 4 and 5) have been presented in [5]. Formulations for MM2 have been included and validated with experimental tests. Formulations for MM3 (shown in Figure 6) have also been included and validated with virtual simulation and experimental tests, as shown in [12]. On the contrary, model MM1 was not analyzed in detail in [5], and formulations for MM1 will be included in the following equations. A comparison between the two models MM1 and MM2 underlines the convenience for using one model instead of the other one.

Figure 8 shows the sketch of model MM1 in a starting position (dashed lines in Figure 8: points C_0, A_0, B_0, D_0) and in motion (continuous lines in Figure 8: points C_1, A_1, B_1, D_1). The mobile part is connected to the fixed part by using four cables, four springs, and four pulleys. Each cable is connected with one spring, interacting with only one pulley. The starting balancing configuration of the mobile part (dashed lines in Figure 8: points C_0, A_0, B_0, D_0) can be perturbed by external resultant forces (F_e) applied in point P, generating the motion of the mobile part. The new balancing configuration (continuous lines in Figure 8: points C_1, A_1, B_1, D_1) and the external applied forces can be found, respectively, with the geometrical analysis of the whole system, and with the analysis of the equilibrium among F_e and the tension on the cables (ΔT_a, ΔT_b, ΔT_c, ΔT_d), obtained by the following equations:

$$\Delta T_a = T_{a11} - T_{a10}; \Delta T_b = T_{b11} - T_{b10}; \Delta T_c = T_{a21} - T_{a20}; \Delta T_d = T_{b21} - T_{b20}; \tag{6}$$

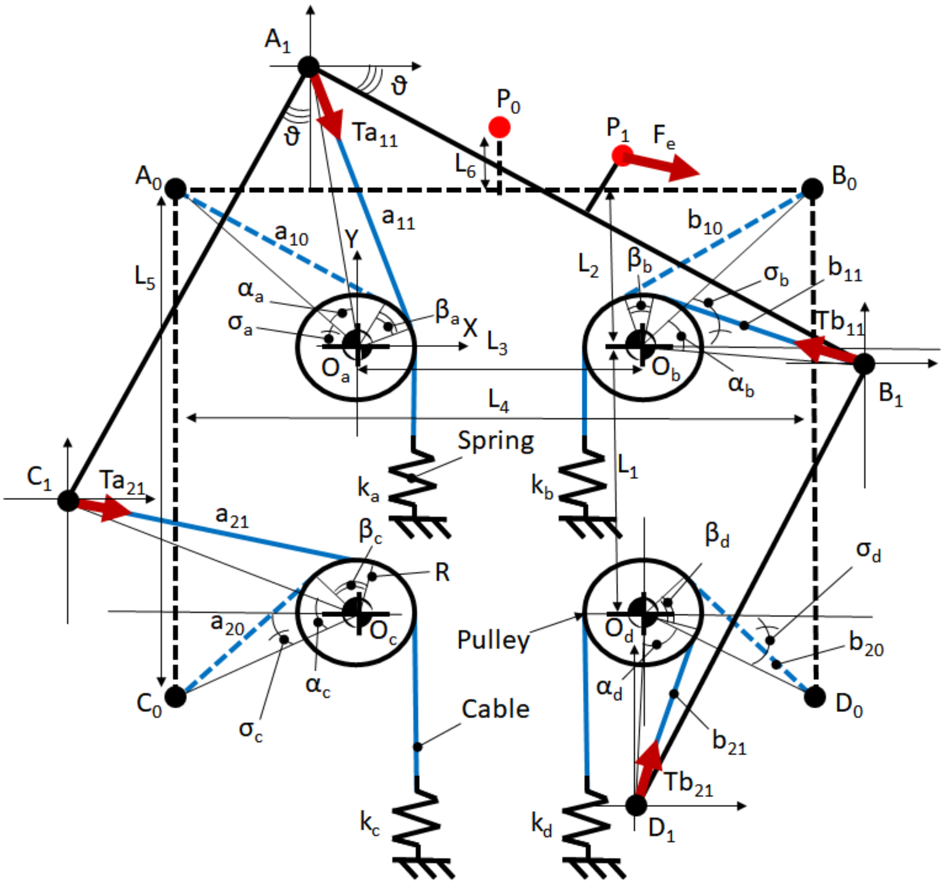

Figure 8. Mechanism model MM1: planar scheme with four cables, four pulleys, and four springs. Mobile part in the starting position (dashed lines: points C_0, A_0, B_0, D_0) and new balancing configuration (continuous lines: points C_1, A_1, B_1, D_1).

The following parameters (shown in Figure 8 and in Equation (7)) will be used in the next few equations:

- Ta_{10}, Tb_{10}, Ta_{20}, Tb_{20} are tensions on four cables in the starting position of the mobile part;
- Ta_{11}, Tb_{11}, Ta_{21}, Tb_{21} are tensions on four cables in the new configuration of the mobile part;
- a_{10}, b_{10}, a_{20}, b_{20} are lengths of the cables in the starting configuration from points A_0, B_0, C_0, D_0 to each tangent of the pulleys centered in O_a, O_b, O_c, O_d;
- a_{11}, b_{11}, a_{21}, b_{21} are lengths of the cables in the new configuration, calculated from the points A_1, B_1, C_1, D_1, respectively, to each tangent of the pulleys centered in O_a, O_b, O_c, O_d;
- R is the radius of the pulleys;
- L_1, L_2, L_3, L_4, L_5, L_6 are the dimensions of the whole system shown in Figure 8;
- α_a, β_a, σ_a, α_b, β_b, σ_b, α_c, β_c, σ_c, α_d, β_d, σ_d are the angles shown in Figure 8;
- k_a, k_b, k_c, k_d are the equivalent stiffness coefficients of the springs and cables in the series;

- δa, δb, δc, δd are displacements of the springs from the starting position to the new balancing configuration;
- δa_0, δb_0, δc_0, δd_0 are displacements of springs in the starting configuration for preloading;
- m_A is the mass of the mobile part;
- g is gravity.

Our assumptions are as follows:

1 All frictions between the cables and pulleys, and pulleys and the shafts of pulleys are zero;
2 $\beta_a = \beta_b = \beta_c = \beta_d = 0$;
3 $k_{eq} = \frac{k_{spring} k_{cable}}{k_{spring} + k_{cable}}$.

Assumption number 1 is appropriate for a virtual environment, like the one presented in this paper.

In assumption number 2, the exact term of β is not known, and it is approximated to zero. One contribution of creating β is given by the displacement of the cable (and spring), and another contribution is created by the geometry of the whole system. In MM2 and MM3, β is not included because pulleys have a small diameter approximated to a point.

In assumption number 3, the equivalent coefficient stiffness (k_{eq}) of the assembled cable-spring system in the series is obtained by the following equation $k_{eq} = \frac{k_{spring} k_{cable}}{k_{spring} + k_{cable}}$, where k_{spring} is the coefficient stiffness of the spring, and k_{cable} is the coefficient stiffness of the cable.

In the base of premises presented above, we can write the following equations:

$$a_{11} = a_{10} + \delta a; \tag{7}$$

$$b_{11} = b_{10} + \delta b; \tag{8}$$

$$a_{21} = a_{20} + \delta c; \tag{9}$$

$$b_{21} = b_{20} + \delta d; \tag{10}$$

$$a_{10} = \sqrt{(\overline{O_a A_0}^2 - R^2)} = b_{10} = \sqrt{(\overline{O_b B_0}^2 - R^2)}; \tag{11}$$

$$a_{20} = \sqrt{(\overline{O_c C_0}^2 - R^2)} = b_{20} = \sqrt{(\overline{O_d D_0}^2 - R^2)}; \tag{12}$$

$$\alpha_a = \beta_a - \arctan(\frac{a_{11}}{R}) + \arctan(\frac{a_{10}}{R}) \tag{13}$$

$$\alpha_b = \beta_b + \arctan(\frac{b_{11}}{R}) - \arctan(\frac{b_{10}}{R}) \tag{14}$$

$$\alpha_c = \beta_c - \arctan(\frac{a_{21}}{R}) + \arctan(\frac{a_{20}}{R}) \tag{15}$$

$$\alpha_d = \beta_d + \arctan(\frac{b_{21}}{R}) - \arctan(\frac{b_{20}}{R}) \tag{16}$$

$$\sigma_a = \sigma_b = \arctan(\frac{2L_2}{L_4 - L_3}); \tag{17}$$

$$\sigma_c = \sigma_d = \arctan(\frac{2(L_5 - L_1 - L_2)}{L_4 - L_3}); \tag{18}$$

$$\Delta T_a = k_a \delta a; \Delta T_b = k_b \delta b; \Delta T_c = k_c \delta c; \Delta T_d = k_d \delta d; \tag{19}$$

$$\begin{aligned} F_{ex} = & -\Delta T_a \sin(\arctan(\frac{R}{a_{11}}) + (\frac{\pi}{2} - (\sigma_a + \alpha_a))) + \Delta T_b \cos(\arctan(\frac{R}{b_{11}}) + (\alpha_b - \sigma_b)) \\ & -\Delta T_c \cos(\alpha_c - \sigma_c) - \Delta T_d \sin(\arctan(\frac{R}{b_{21}}) + (\sigma_d + \alpha_d - \frac{\pi}{2})); \end{aligned} \tag{20}$$

$$F_{ey} = -\Delta T_a \cos(\arctan(\frac{R}{a_{11}}) + (\frac{\pi}{2} - (\sigma_a + \alpha_a))) + \Delta T_b \sin(\arctan(\frac{R}{b_{11}}) + (\alpha_b - \sigma_b)) \\ -\Delta T_c \sin(\alpha_c - \sigma_c) + \Delta T_d \cos(\arctan(\frac{R}{b_{21}}) + (\sigma_d + \alpha_d - \frac{\pi}{2}) - m_A g; \tag{21}$$

$$F_e = \sqrt{F_{ex}^2 + F_{ey}^2}; \tag{22}$$

By using Equation (6), tension on the cables can be found, and Equations (20)–(22) permit the determination of external forces on point P.

2.4. Comparison Between MM1 and MM2 Models

Figure 9 on the left shows the planar scheme of model MM2. A preliminary comparison between MM1 and MM2 (respectively, shown in the two Figures 8 and 9 on the left), underlines that the formulations for model MM2 include an added advantage with respect to the equations shown above (for MM1) because the boundary conditions in MM2 simplify the entire calculation. In the new balancing configuration in the continuous lines, anchor points of the cables with the mobile part for MM1 are four (A_1, B_1, C_1, D_1) but for MM2 are reduced to two (E_1, F_1). This boundary condition helps to propose a more robust solution for MM2 with respect to MM1, increasing the stability of the whole system. The formulation of MM2 was discussed in detail in [5], starting from Equation (5) shown above. The projection of cables in the starting position of model MM1 (Figure 9 on the right: orange dashed lines) can cross at four points (W_1, N_1, V_1, H_1) near the total center of rotation M_c. This means that the proposed geometrical configuration for MM1 requests more external interventions in order to have equilibrium. On the contrary, the projection of cables in the starting position of model MM2 (Figure 9 on the right: gray dashed lines) can cross only at two points (W_2, V_2), not near the total center of rotation M_c. This means that the proposed geometrical configuration for MM2 requests minor external interventions with respect to MM1 in order to have equilibrium. This observation, also noted in [5], is confirmed in this paper and in the results of virtual simulations presented in the next few sections.

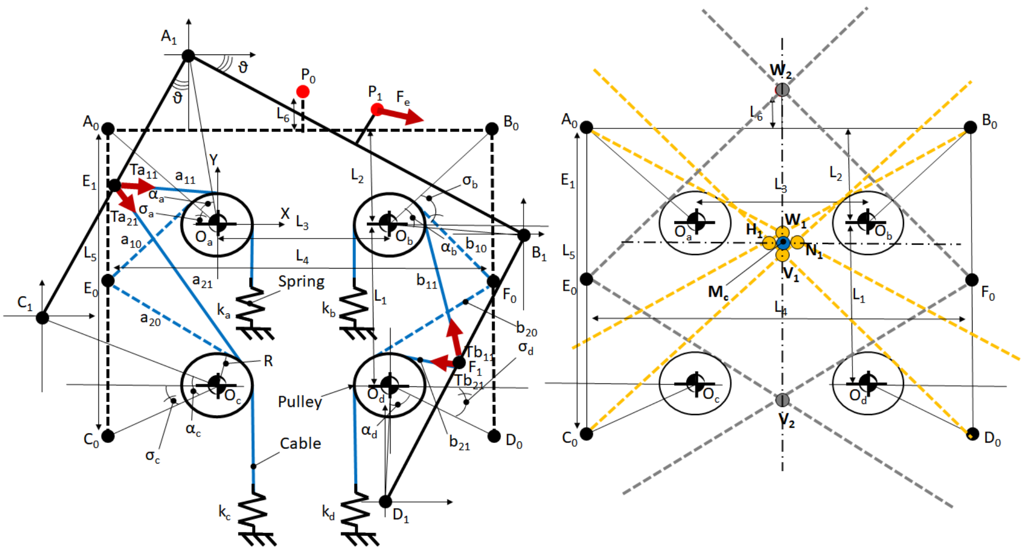

Figure 9. Left: planar scheme with four cables, four pulleys, and four springs for mechanism model MM2. Mobile part in the starting position (dashed lines: points C_0, E_0, A_0, B_0, F_0, D_0) and new balancing configuration (continuous lines: points C_1, E_1, A_1, B_1, F_1, D_1). **Right**: scheme for the comparison between MM1 and MM2.

3. Physical Implementation of MM2

3.1. Test Benches for MM2

Test benches for the implementation of the formulations for MM2 were conceived with two fundamental parts: one external hollow cylinder (mobile part A) and one internal part (fixed part B). The external hollow cylinder is connected with the internal part by using cables.

We conceived an innovative formula for eight cables, shown in [5], able to measure (as an output) external loads (applied on the tip of the mobile part) and its position and rotation, using as input the displacement of each spring connected to each cable. MM2 is the model used for the conceived formulation.

Our final objective is to reduce the dimensions of the cable-driven sensitive mechanism in order to include it in one part of the tube of the MIRI (near the forceps). In this case, the external dimensions of the sensitive mechanisms must be not more than 8 mm. However, in order to validate the formulation presented in [5], two test benches were developed (for MM2) with bigger dimensions with respect to 8 mm. The formulation presented in [5] is able to describe well the mechanical behavior of the two different test benches shown in Figures 10 and 11, which used the same type of spring, with an external diameter of 9.4 mm, number of wraps 25, stiffness coefficient 0.6786 N/mm, initial length of spring 24.8 mm, and diameter of wire 1 mm. The diameter of the cable in nylon is 0.6 mm.

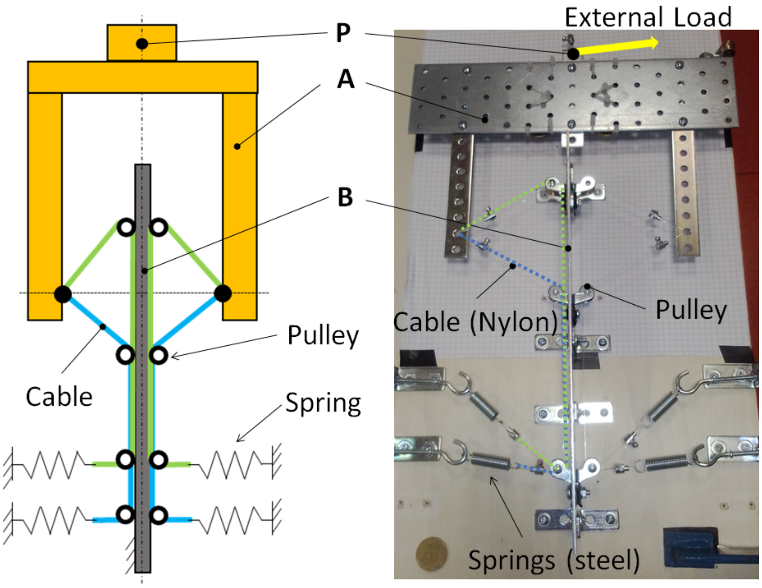

Figure 10. Test bench I for validation of the formulation presented in [5] (MM2) with the application in the plane: scheme (**left**) and realized prototype in metal (**right**).

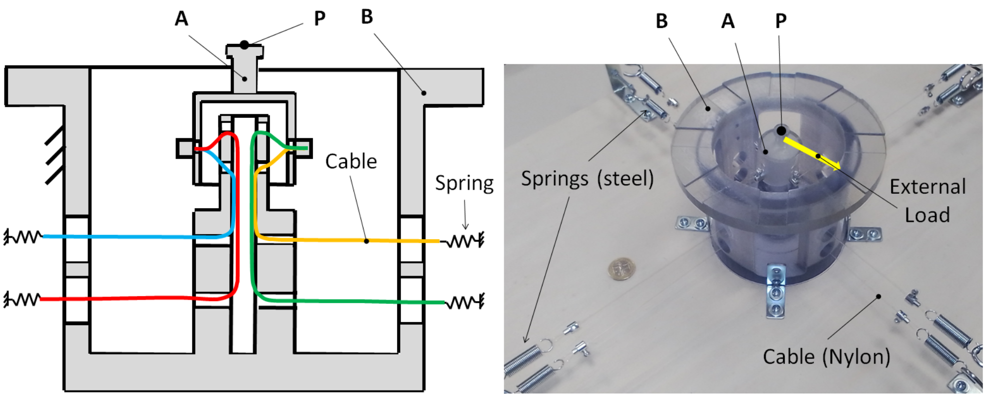

Figure 11. Test bench II for validation of the formulation presented in [5] (MM2) with the application in the space: sketch of the axial section (**left**) and realized prototype with 3D printer (**right**).

3.2. Procedure for Experimentation

Part B of the test bench prototypes is fixed to the plane. Part A is connected to part B using cables. Cables are attached to part A after passing through holes of part B (see Figure 11) or through pulleys (see Figure 10). An external load has been applied on part A by adding different weights in point P. In each experiment, about the same process was performed:

1 Connection of cables with the mobile part;
2 Connection of cables with springs, passing around the pulleys (or holes);
3 Calibration of the mechanism in the initial position by using screws;
4 Measurement of the length of springs;
5 Application of loads connected (by a cable) to point P;
6 Measurement of the new length of springs;
7 Measurement of the displacement of point P.

External loads applied to the planar test bench I of Figure 10 are as follows: 6.46 N, 7.48 N, 8.49 N, 9.85 N, 10.94 N. The following resultant forces are applied in the test bench II of Figure 11: 3.25 N, 4.26 N, 5.27 N, 6.46 N, 7.48 N, 8.49 N, 9.57 N. A comparison between the measured forces (MF) and calculated forces (CF) with the formulation presented in [5] validated model MM2. In order to also validate the formulation of MM1 and MM2, we performed virtual simulations presented in the following section.

4. Multibody Design and Control of MM1 and MM2

4.1. Design of Multi-Body Models

In this section, the cable-driven multi-body analysis and design optimization of test benches for MIRIs are proposed. The multi-body simulation was performed by using MATLAB®, Simulink®, and Simscape™ Multibody™.

In order to reduce the dimensions of our proposed sensitive systems, and to implement it in MIRIs, we designed smaller systems. Figures 12 and 13, respectively, show multi-body models of MM1 and MM2. In the planar system, mobile part A is connected to four motors (attached to fixed part B) by using cables and pulleys.

Figure 14 shows multi-body model MM2 with the same dimensions implemented in the planar test bench I used for experimentation in [5] and shown in Figure 10. Details on the used equations can be found in [5]. The external applied force is found by using Equation (5). All dimensions are shown in Figures 12, 13, and 14.

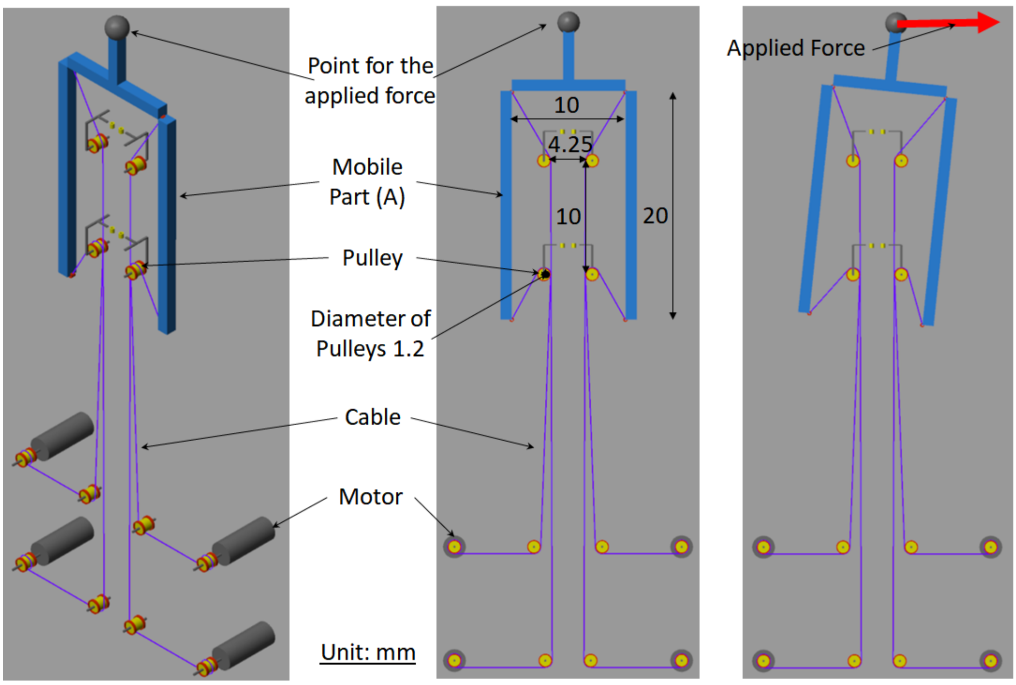

Figure 12. Multi-body model MM1 in a reduced scale.

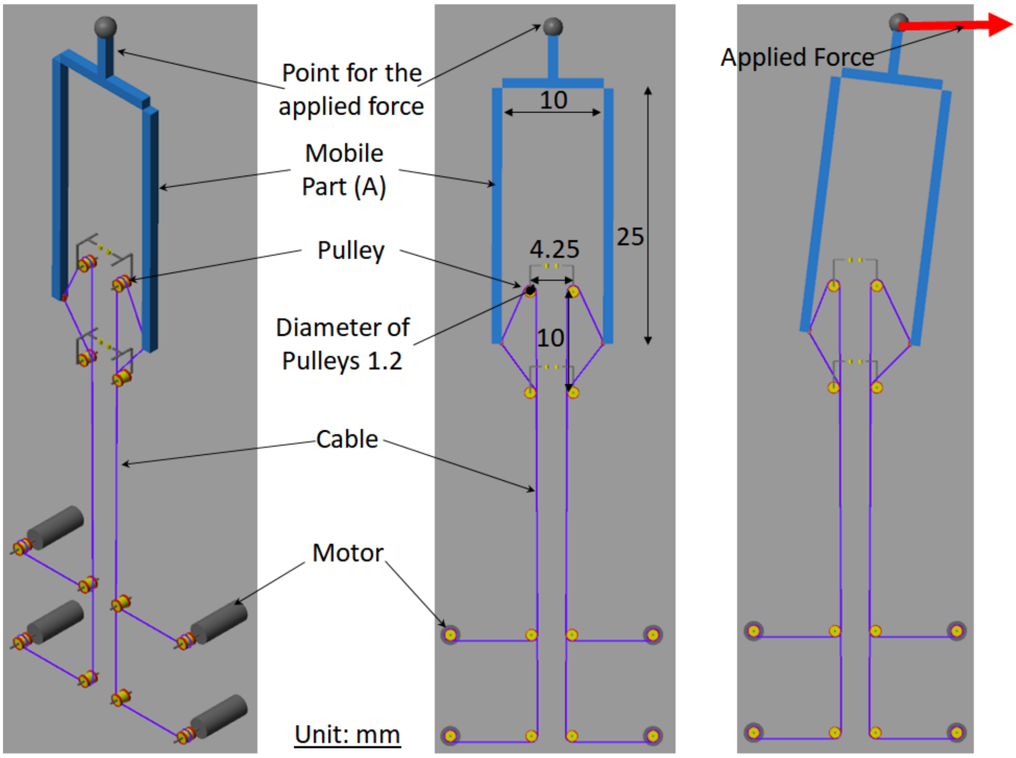

Figure 13. Multi-body model MM2 in a reduced scale.

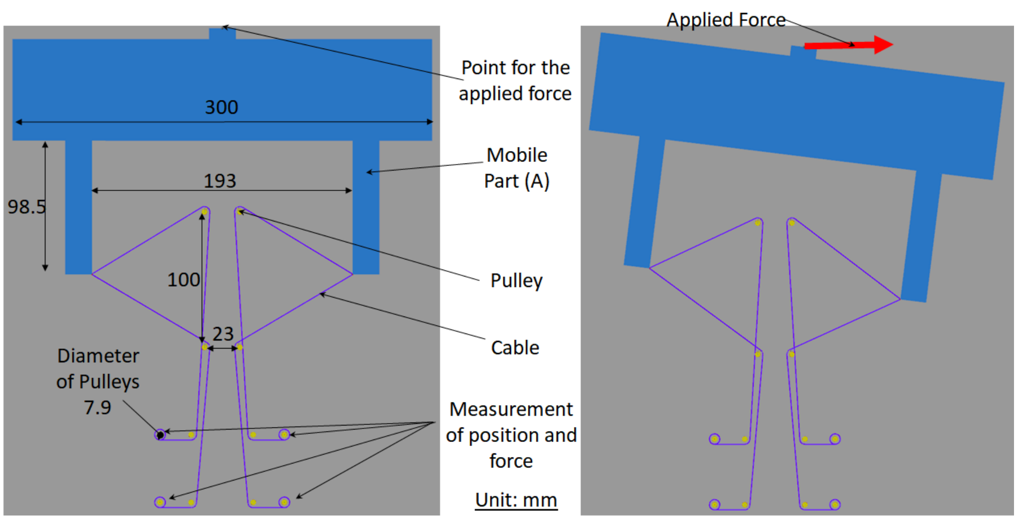

Figure 14. Multi-body model MM2 implemented in the planar test bench I with big dimensions.

4.2. General Control Architectures for Each Model

Our proposed architectures for models MM1, MM2, and MM3 (shown in Figures 15 and 16) are able to control and/or to measure the motion of part C, where forceps are attached (see Figure 3), and the interaction forces on the forceps by using only the measure of the revolution of motors (or the displacement of each spring at the end of each cable). Figures 15 and 16 show the control blocks for the sensing and actuation architectures applied to each model presented above and in our previous works [5,12].

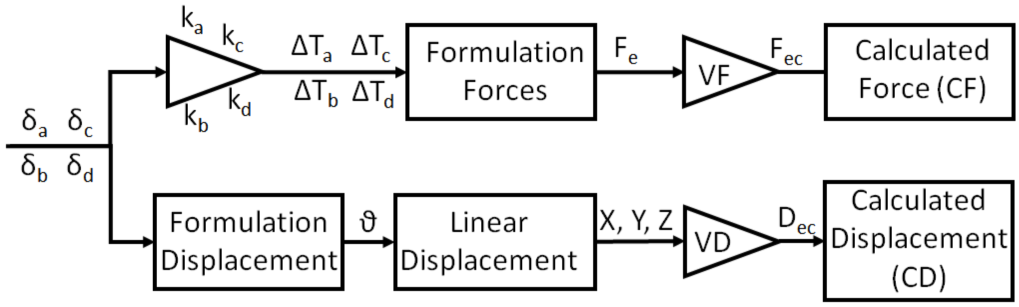

Figure 15. Sensing control architecture for each model. δ_a, δ_b, δ_c, δ_b are displacements of springs; k_a, k_b, k_c, k_d are equivalent stiffness coefficients, ΔT_a, ΔT_b, ΔT_c, ΔT_d are tensions on cables; F_{ec} is the calculated external force; θ is the angular displacement of the mobile part with respect to the fixed part; VF is the force amplification value and VD is the displacement amplification value.

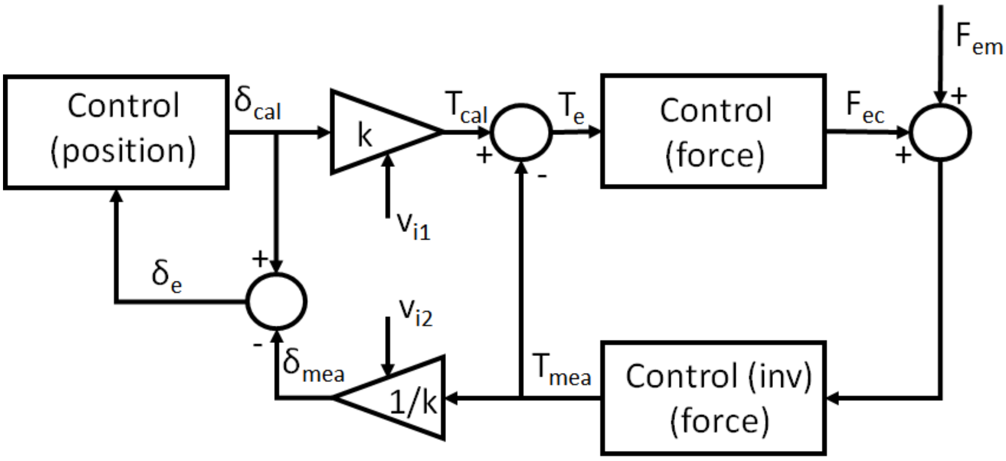

Figure 16. Actuation control architecture for each model. δe is the error between measured (δ_{mea}) and calculated (δ_{cal}) displacement of the spring; T_e is the error between measured (T_{mea}) and calculated (T_{cal}) tensions on cables; k is the equivalent stiffness coefficient; F_{ec} is the calculated external force; F_{em} is the measured external force; v_{i1} and v_{i2} are input to have variable coefficients of stiffness. In this work, the equivalent stiffness coefficient k is constant.

Figure 15 shows the sensitive control architecture. The displacements of springs (δ_a, δ_b, δ_c, δ_b) (or the displacement of the revolution of motors, obtained by δ_a, δ_b, δ_c, δ_b) are used to calculate the applied forces and motion on the mobile part. For model MM1, studied in the last section, Equation (22) allows for the calculation of the external forces (F_{ec}). ΔT_a, ΔT_b, ΔT_c, ΔT_d are the tensions on cables and k_a, k_b, k_c, k_d are the equivalent stiffness coefficients of springs and cables. Calculated forces (CF) and displacements (CD) are obtained, respectively, including two proportional values: force amplification value (VF) and displacement amplification value (VD).

If the model is used like an actuated system, inputs to the system are the revolute motions of motors (used instead of springs). A correct combination of the motion of motors permits for the movement of part C, where forceps are attached (see Figure 3). On the contrary, if the model is used like a sensitive system, the motion and forces applied on part C, where forceps are attached (see Figure 3), can be evaluated by the combination of motions and torques on motors.

Figure 16 shows the control architecture for the actuated system. Calculated tensions on cables (T_{cal}) are used to evaluate the error between the measured one (T_{mea}). This error helps to reduce the gap between the measured and calculated external forces (F_{em} and F_{ec}). The error between the measured displacement (δ_{mea}) and the calculated one (δ_{cal}) allows for the reduction of the gap in the prevision of motion of the mobile part.

5. Results and Discussion

Figure 17 shows the results of a simulation if a measured force (MF) of 1 N is applied to the sphere of multi-body model MM1, shown in Figure 12. On the top left of Figure 17, forces are calculated (CF) modifying the damping coefficient c from 0.2 Nms/deg to 3 Nms/deg and using stiffness coefficient $k = 0.0033$ Nmm/deg for the four revolute joints. In the multi-body environment the cable is assumed inextensible, and it is not included in the calculation of the equivalent stiffness coefficient. On the top right of Figure 17, forces are calculated (CF) with a fixed damping coefficient $c = 1$ Nms/deg and modifying the stiffness coefficient k from 0.0033 Nmm/deg to 330 Nmm/deg for the four revolute joints. In the center (down), the simulation of model MM1 is presented with six different measured force inputs: 1 N, 2 N, 3 N, 4 N, 5 N, 6 N. Forces are calculated (CF) with damping coefficient $c = 1$ Nms/deg and stiffness coefficient $k = 0.0033$ Nmm/deg and using the following coefficients for displacement $VD = 0.074$ and force $VF = 0.137$. Results presented in Figure 17 underline that the formulation conceived for MM1 requests high damping to converge, and high forces cannot be managed correctly. These results confirm the analysis performed in the last section and shown in Figure 9, in which the equilibrium of model MM1 was noted as not stable for its geometrical characteristics with respect to model MM2.

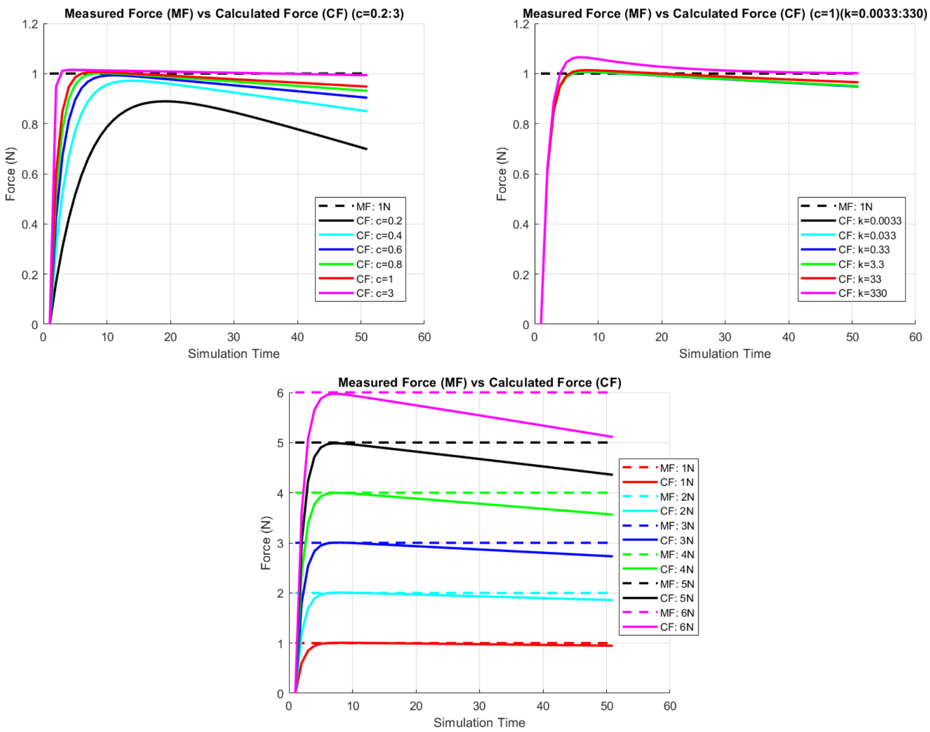

Figure 17. Simulation of model MM1 shown in Figure 12 with 1 N of measured force (MF). Left (top): calculated force (CF) with damping coefficient c variable from 0.2 Nms/deg to 3 Nms/deg and fixed stiffness coefficient $k = 0.0033$ Nmm/deg for the four revolute joints. Right (top): calculated force (CF) with fixed damping coefficient $c = 1$ Nms/deg and variable stiffness coefficient k from 0.0033 Nmm/deg to 330 Nmm/deg for the four revolute joints. Center (down): simulation of model MM1 with six different measured force inputs: 1 N, 2 N, 3 N, 4 N, 5 N, 6 N. Forces are calculated (CF) with damping coefficient $c = 1$ Nms/deg and stiffness coefficient $k = 0.0033$ Nmm/deg. $VD = 0.074$; $VF = 0.137$.

Figure 18 shows the virtual simulation of model MM2 (shown in Figure 13) with 1 N of measured force (MF). In the top of the figure, forces are calculated (CF) with a variable damping coefficient c from 0.2 Nms/deg to 3 Nms/deg and a fixed stiffness coefficient $k = 0.0033$ Nmm/deg for the four revolute joints. In the multi-body environment the cable is assumed inextensible, and it is not included in the calculation of the equivalent stiffness coefficient. In the lower part of the figure, forces are calculated (CF) with fixed damping coefficient $c = 1$ Nms/deg and variable stiffness coefficient k from 0.0033 Nmm/deg to 330 Nmm/deg for the four revolute joints. The following coefficients for displacement and force are used: $VD = 0.5$, $VF = 0.83$.

On the contrary to model MM1, model MM2 is stable and more efficient for use as the next generation of MIRIs. This result was also noted and underlined in [5]. This is also confirmed in Figure 19, in which six different measured force inputs are applied to MM2. It can be seen that force and displacement errors are very low, underlining the very good quality of model MM2. The quality of model MM2 is also validated with the multi-body model with bigger dimensions, shown in Figure 14, for test bench I, shown in Figure 10 and presented in [5]. Figure 20 confirms the very good quality of the formulation presented in [5]. The five external loads applied to the mobile part in Figure 21 are the same applied in the experimental tests for test bench I presented in [5].

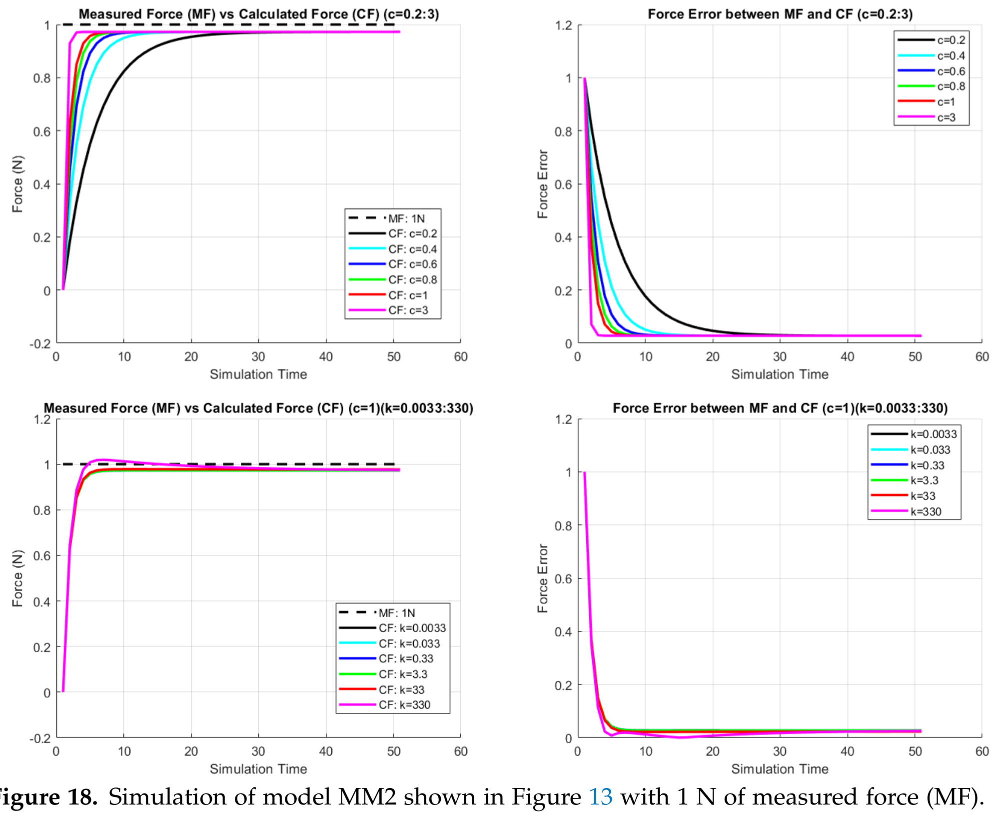

Figure 18. Simulation of model MM2 shown in Figure 13 with 1 N of measured force (MF). Top: calculated force (CF) with damping coefficient c variable from 0.2 Nms/deg to 3 Nms/deg and fixed stiffness coefficient $k = 0.0033$ Nmm/deg for the four revolute joints. Left (top): measured (MF) and calculated (CF) forces; right (top): force error between MF and CF. Down: calculated force (CF) with fixed damping coefficient $c = 1$ Nms/deg and variable stiffness coefficient k from 0.0033 Nmm/deg to 330 Nmm/deg for the four revolute joints. Left (down): measured (MF) and calculated (CF) forces; right (down): force error between MF and CF. $VD = 0.5$; $VF = 0.83$.

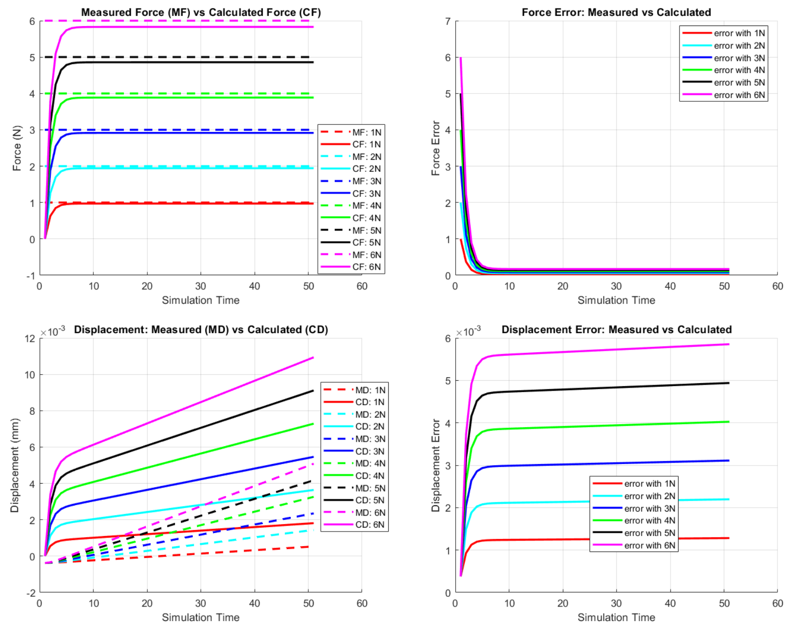

Figure 19. Simulation of model MM2 shown in Figure 13 with six different measured force inputs: 1 N, 2 N, 3 N, 4 N, 5 N, 6 N. Forces are calculated (CF) with fixed damping coefficient $c = 1$ Nms/deg and stiffness coefficient $k = 0.0033$ Nmm/deg. Left (top): measured (MF) and calculated (CF) forces; right (top): error between measured and calculated forces. Left (down): measured (MD) and calculated (CD) displacements; right (down): error between measured and calculated displacements. $VD = 0.5$; $VF = 0.83$.

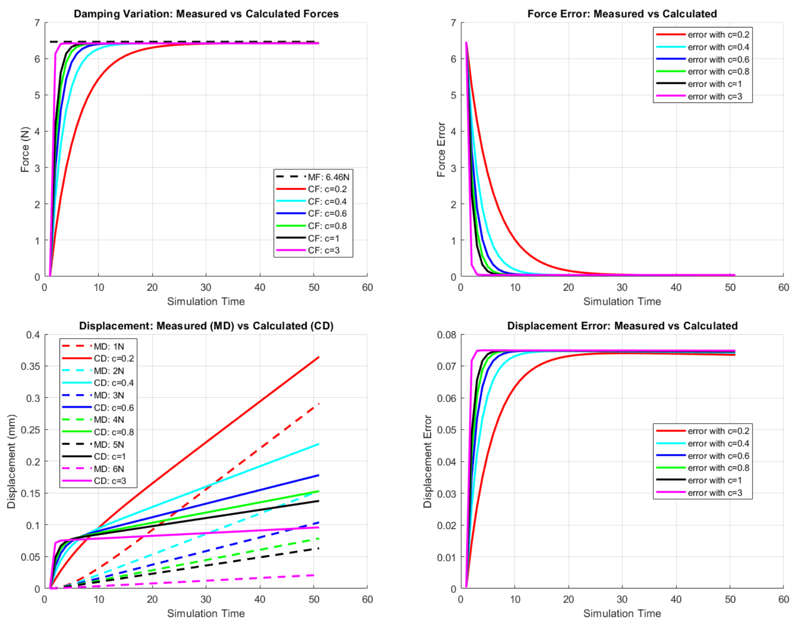

Figure 20. Simulation of model MM2 implemented in test bench I shown in Figures 14 and 10 with measured force input: 6.46 N. Top: calculated force (CF) with damping coefficient c variable from 0.2 Nms/deg to 3 Nms/deg and stiffness coefficient $k = 0.1416$ Nmm/deg for the four revolute joints. k is the stiffness of the motor joints, obtained by the same stiffness coefficient of the spring used in test bench I in [5] ($k_{spring} = 0.6786$ N/mm) ($k = (2\pi k_{eq} R^2)/360$). Left (top): measured (MF) and calculated (CF) forces; right (top): force error between MF and CF; left (down): measured (MD) and calculated (CD) displacements; right (down): displacement error between MD and CD. $VD = 0.25$; $VF = 1.9$.

In line with the results presented in [5] and confirmed with virtual simulations in this paper, MM2 is confirmed to be a very good model to be used for implementation in MIRIs. Figure 22 shows the new test benches designed and realized (with a 3D printer) in different reduced scales for the next experimentation on model MM2. Pictures of realized test benches are shown with reduced-scale prototypes with the diameter J of around 28 mm, 15 mm, and 7 mm.

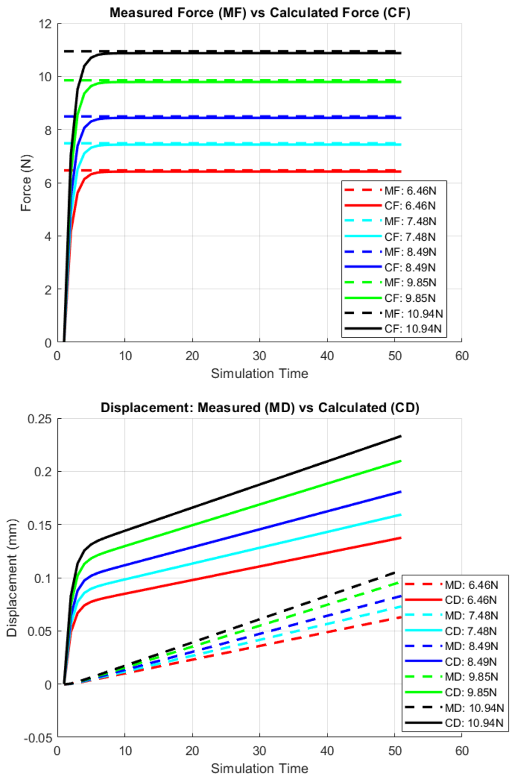

Figure 21. Simulation of the model MM2 implemented in test bench I shown in Figures 14 and 10 with five measured force inputs: 6.46 N, 7.48 N, 8.49 N, 9.85 N, 10.94 N, as shown in [5]. Top: calculated force (CF) with damping coefficient $c = 1$ Nms/deg and stiffness coefficient $k = 0.1416$ Nmm/deg for the four revolute joints. k is the stiffness of the motor joints, obtained by the same stiffness coefficient of the spring used in test bench I in [5] ($k_{spring} = 0.6786$ N/mm) ($k = (2\pi k_{eq} R^2)/360$). Left (top): measured (MF) and calculated (CF) forces; right (top): force error between MF and CF; left (down): measured (MD) and calculated (CD) displacements; right (down): displacement error between MD and CD. $VD = 0.25$; $VF = 1.9$.

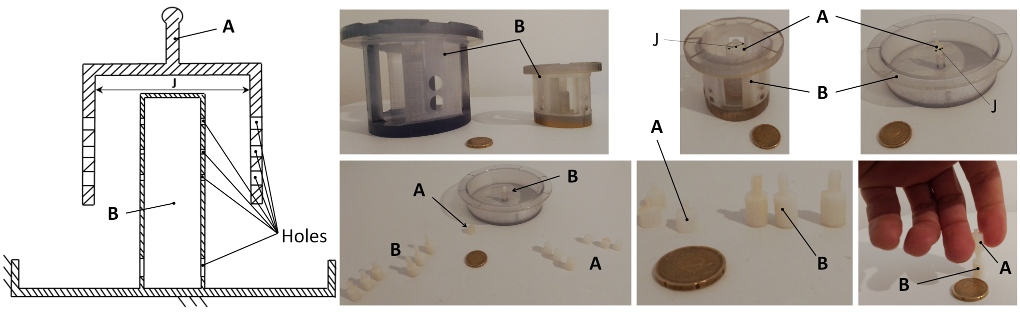

Figure 22. New test benches in different reduced scales, designed and realized with a 3D printer for the next experimentation on model MM2. A is the mobile part and B is the fixed part. Left: sketch of the section of test benches. Right (top): pictures of realized test benches, as shown in Figure 11, with $J = 28$ mm, $J = 15$ mm, and $J = 7$ mm. Right (down): parts A and B for implementation on MIRI, as shown in Figure 3.

6. Conclusions

In this paper, we presented an evolution of our recent works on sensing cable-driven mechanism models. Two mechanism models are compared by using a virtual multi-body simulation. Results confirm the preliminary hypotheses performed on the two models. One model is more appropriate for use in the construction of minimally invasive robotic instruments because of its capability to maintain balance. Future works will be focused on performing more tests at a reduced scale. Some prototypes are developed, and further experiments on minimally invasive robotic instruments are planned for the next future.

Author Contributions: Conceptualization, G.G.M.; methodology, G.G.M.; software, G.G.M.; validation, G.G.M.; formal analysis, G.G.M.; investigation, G.G.M.; resources, G.G.M. and P.F.; data curation, G.G.M.; writing—original draft preparation, G.G.M.; writing—review and editing, G.G.M. and P.F.; visualization, G.G.M. and P.F.; supervision, G.G.M. and P.F.; project administration, G.G.M. and P.F.; funding acquisition, P.F. All authors have read and agreed to the published version of the manuscript.

Funding: This work was supported in part by the European Union Grants ERC-ADG N. 742671, ARS (Autonomous Robotic Surgery) project. URL: https://www.ars-project.eu, accessed on 19 February 2024.

Institutional Review Board Statement: Not applicable.

Informed Consent Statement: Not applicable.

Data Availability Statement: Data is contained within the article.

Conflicts of Interest: The authors declare no conflicts of interest.

Abbreviations

The following abbreviations are used in this manuscript:

FBG	Fiber Bragg Gratings
MEMS	Micro-Electro-Mechanical Systems
MIRI	Minimally Invasive Robotic Instrument
dVRK	da Vinci Research Kit
FF	Force Feedback
HF	Haptic Feedback
MF	Measured Force
CF	Calculated Force
MD	Measured Displacement
CD	Calculated Displacement
VF	Force Amplification Value
VD	Displacement Amplification Value

References

1. Iguchi, K.; Numata, M.; Shiozawa, M.; Kazama, K.; Sawazaki, S.; Katayama, Y.; Numata, K.; Higuchi, A.; Godai, T.; Sugano, N.; et al. Analysis of surgical outcomes of laparoscopic versus open surgery for locally advanced mid-transverse colon cancer. *Langenbeck's Arch. Surg.* **2023**, *408*, 222. [CrossRef] [PubMed]
2. Tonutti, M.; Elson, D.S.; Yang, G.Z.; Darzi, A.W.; Sodergren, M.H. The role of technology in minimally invasive surgery: State of the art, recent developments and future directions. *Postgrad. Med. J.* **2017**, *93*, 159–167. [CrossRef] [PubMed]
3. Zhang, W.; Li, H.; Cui, L.; Li, H.; Zhang, X.; Fang, S.; Zhang, Q. Research progress and development trend of surgical robot and surgical instrument arm. *Int. J. Med. Robot.* **2021**, *17*, e2309. [CrossRef] [PubMed]
4. Muscolo, G.G.; Fiorini, P. Force-Torque Sensors for Minimally Invasive Surgery Robotic Tools: An overview. *IEEE Trans. Med. Robot. Bionics* **2023**, *5*, 458–471. [CrossRef]
5. Muscolo, G.G.; Fiorini, P. A New Cable-Driven Model for Under-Actuated Force–Torque Sensitive Mechanisms. *Machines* **2023**, *11*, 617. [CrossRef]
6. Muscolo, G.G.; Hashimoto, K.; Takanishi, A.; Dario, P. A Comparison between Two Force-Position Controllers with Gravity Compensation Simulated on a Humanoid Arm. *J. Robot.* **2013**, *2013*, 256364. [CrossRef]
7. Hamida, I.B.; Laribi, M.A.; Mlika, A.; Romdhane, L.; Zeghloul, S.; Carbone, G. Multi-objective optimal design of a cable driven parallel robot for rehabilitation tasks. *Mech. Mach. Theory* **2021**, *156*, 104141. [CrossRef]

8. Pinto, A.M.; Moreira, E.; Lima, J.; Sousa, J.P.; Costa, P. A cable-driven robot for architectural constructions: A visual-guided approach for motion control and path-planning. *Auton. Robot.* **2017**, *41*, 1487–1499. [CrossRef]
9. Mishra, U.A.; Caro, S. Forward kinematics for suspended under-actuated cable-driven parallel robots with elastic cables: A neural network approach. *J. Mech. Robot.* **2022**, *14*, 041008. [CrossRef]
10. Min, S.; Yi, S. Development of cable-driven anthropomorphic robot hand. *IEEE Robot. Autom. Lett.* **2021**, 6, 1176–1183. [CrossRef]
11. Zhang, B.; Shang, W.; Cong, S.; Li, Z. Coordinated dynamic control in the task space for redundantly actuated cable-driven parallel robots. *IEEE/ASME Trans. Mechatronics* **2020**, *26*, 2396–2407. [CrossRef]
12. Muscolo, G.G.; Fiorini, P. A Planar Cable-Driven Under-Sensing Model to Measure Forces and Displacements. *Machines* **2024**, *12*, 129. [CrossRef]
13. Lin, B.; Xu, W.; Li, W.; Yuan, H.; Liang, B. Ex Situ Sensing Method for the End-Effector's Six-Dimensional Force and Link's Contact Force of Cable-Driven Redundant Manipulators. *IEEE Trans. Ind. Inform.* **2024**. [CrossRef]
14. Francis, C.; Sato, T.; Okuyama, T.; Tanaka, M. A cable driven robotic palpation system with contact force sensing based on cable tension observation. *Int. J. Med. Robot. Comput. Assist. Surg.* **2022**, *18*, e2435. [CrossRef] [PubMed]
15. Chen, Q.; Lin, Q.; Wei, G.; Ren, L. Tension vector and structure matrix associated force sensitivity of a 6-DOF cable-driven parallel robot. *Proc. Inst. Mech. Eng. Part C J. Mech. Eng. Sci.* **2022**, *236*, 100–114. [CrossRef]
16. Guagliumi, L.; Berti, A.; Monti, E.; Fabritius, M.; Martin, C.; Carricato, M. Force-Sensor-Free Implementation of a Hybrid Position–Force Control for Overconstrained Cable-Driven Parallel Robots. *Robotics* **2024**, *13*, 25. [CrossRef]
17. Mattioni, V.; Idà, E.; Carricato, M. Force-distribution sensitivity to cable-tension errors in overconstrained cable-driven parallel robots. *Mech. Mach. Theory* **2022**, *175*, 104940. [CrossRef]
18. Paty, T.; Binaud, N.; Wang, H.; Segonds, S. Sensitivity Analysis of a Suspended Cable-Driven Parallel Robot to Design Parameters. *ASME. J. Mech. Robot.* **2023**, *15*, 061001. [CrossRef]
19. Fabritius, M.; Rubio-Gómez, G.; Martin, C.; Santos, J.C.; Kraus, W.; Pott, A. A nullspace-based force correction method to improve the dynamic performance of cable-driven parallel robots. *Mech. Mach. Theory* **2023**, *181*, 105177. [CrossRef]
20. Meccariello, G.; Faedi, F.; AlGhamdi, S.; Montevecchi, F.; Firinu, E.; Zanotti, C.; Cavaliere, D.; Gunelli, R.; Taurchini, M.; Amadori, A.; et al. An experimental study about haptic feedback in robotic surgery: May visual feedback substitute tactile feedback? *J. Robot. Surg.* **2016**, *10*, 57–61. [CrossRef]
21. Yang, Y.; Li, J.; Kong, K.; Wang, S. Design of a dexterous robotic surgical instrument with a novel bending mechanism. *Int. J. Med. Robot. Comput. Assist. Surg.* **2022**, *18*, E2334. [CrossRef] [PubMed]
22. Wu, Z.; Zhu, C.; Ding, Y.; Wang, Y.; Xu, B.; Xu, K. A robotic surgical tool with continuum wrist, kinematically optimized curved stem, and collision avoidance kinematics for single port procedure. *Mech. Mach. Theory* **2022**, *173*, 104863. [CrossRef]
23. Kim, L.H.; Bargar, C.; Che, Y.; Okamura, A.M. Effects of master-slave tool misalignment in a teleoperated surgical robot. In Proceedings of the 2015 IEEE International Conference on Robotics and Automation (ICRA), Seattle, WA, USA, 26–30 May 2015.
24. Tzemanaki, A.; Fracczak, L.; Gillatt, D.; Koupparis, A.; Melhuish, C.; Persad, R.; Rowe, E.; Pipe, A.G.; Dogramadzi, S. Design of a multi-DOF cable-driven mechanism of a miniature serial manipulator for robot-assisted minimally invasive surgery. In Proceedings of the 2016 6th IEEE International Conference on Biomedical Robotics and Biomechatronics (BioRob), Singapore, 26–29 June 2016; pp. 55–60.
25. Mylonas, G.P.; Vitiello, V.; Cundy, T.P.; Darzi, A.; Yang, G.-Z. CYCLOPS: A versatile robotic tool for bimanual single-access and natural-orifice endoscopic surgery. In Proceedings of the 2014 IEEE International Conference on Robotics and Automation (ICRA), Hong Kong, China, 31 May–7 June 2014, pp. 2436–2442. [CrossRef]
26. Xiong, L.; Guo, Y.; Jiang, G.; Zhou, X.; Jiang, L.; Liu, H. Six-Dimensional Force/Torque Sensor Based on Fiber Bragg Gratings With Low Coupling. *IEEE Trans. Ind. Electron.* **2021**, *68*, 4079–4089. [CrossRef]
27. Golahmadi, A.K.; Khan, D.Z.; Mylonas, G.P.; Marcus, H.J. Tool-tissue forces in surgery: A systematic review. *Ann. Med. Surg.* **2021**, *65*, 102268. [CrossRef]
28. Wang, H.; Wang, W.; Du, Z.; Gao, Y. Design of 3D force perception system of surgical robots based on fiber Bragg grating. In *MATEC Web of Conferences*; EDP Sciences: Les Ulis, France, 2021; Volume 336.
29. Cheng, A.J.; Wu, L.; Sha, Z.; Chang, W.; Chu, D.; Wang, C.H.; Peng, S. Recent advances of capacitive sensors: Materials, microstructure designs, applications, and opportunities. *Adv. Mater. Technol.* **2023**, *8*, 2201959. [CrossRef]
30. Sarwar, M.S.; Ishizaki, R.; Morton, K.; Preston, C.; Nguyen, T.; Fan, X.; Dupont, B.; Hogarth, L.; Yoshiike, T.; Qiu, R.; et al. Touch, press and stroke: A soft capacitive sensor skin. *Sci. Rep.* **2023**, *13*, 17390. [CrossRef]
31. Shi, H.; Zhang, B.; Mei, X.; Song, Q. Realization of force detection and feedback control for slave manipulator of master/slave surgical robot. *Sensors* **2021**, *21*, 7489. [CrossRef]
32. Puangmali, P.; Althoefer, K.; Seneviratne, L.D.; Murphy, D.; Dasgupta, P. State-of-the-art in force and tactile sensing for minimally invasive surgery. *IEEE Sens. J.* **2008**, *8*, 371–381. [CrossRef]

33. Schäfer, M.; Glöckner, A.; Friedrich, G.; Meiringer, J.; Pott, P. Measuring interaction forces in surgical telemanipulation using conventional instruments. *Robotica* **2023**, *41*, 1335–1347. [CrossRef]
34. Ranganath, R.; Nair, P.S.; Mruthyunjaya, T.S.; Ghosal, A. A force–torque sensor based on a Stewart Platform in a near-singular configuration. *Mech. Mach. Theory* **2004**, *39*, 971–998. [CrossRef]